Catalysis Science & Technology

Composition Sensitive Selectivity and Activity of Electrochemical Carbon Dioxide Reduction on Pd-Cu Solid-Solution Alloy Nanoparticles

Journal:	*Catalysis Science & Technology*
Manuscript ID	CY-ART-05-2023-000748.R1
Article Type:	Paper
Date Submitted by the Author:	12-Jul-2023
Complete List of Authors:	Todoroki, Naoto; Tohoku University, Graduate School of Environmental Studies; Tohoku University Ishijima, Masanao; Tokyo Metropolitan University, Department of Applied Chemistry for Environment Cuya Huaman, Jhon; Tohoku University, Department of Environmental Studies Tanaka, Yuto; The University of Shiga Prefecture, Department of Materials Science Balachandran, Jeyadevan; Tohoku University, Department of Environmental Studies

ARTICLE

Composition Sensitive Selectivity and Activity of Electrochemical Carbon Dioxide Reduction on Pd-Cu Solid-Solution Alloy Nanoparticles

Received 00th January 20xx,
Accepted 00th January 20xx

DOI: 10.1039/x0xx00000x

Naoto Todoroki,*[a] Masanao Ishijima,*[b] Jhon L. Cuya Huaman,[a] Yuto Tanaka[c] and Jeyadevan Balachandran[a]

The effect of alloying on the electrochemical carbon dioxide reduction reaction (CO_2RR) has been investigated to improve the electrocatalytic performance. Pd-Cu bimetallic alloys show high selectivity for formate and CO as CO_2RR products. However, the change of selectivity and activity with the alloy composition and applied potential is unclear. This study investigates the CO_2RR properties of Pd-Cu solid-solution bimetallic alloy nanoparticles (NPs) and discusses the effects of composition and potential for formate and CO. Composition-controlled Pd_xCu_{100-x} (x = 73, 64, 56, and 46) NPs are synthesized via alcohol reduction. Microstructural and composition analyses reveal that all alloy NPs have a well-controlled composition with solid-solution (alloy) structures, which are suitable for discussing the composition effect. The Pd_xCu_{100-x} NPs exhibit enhanced selectivity for formate irrespective of the alloy composition. Notably, the $Pd_{64}Cu_{36}$ presents a selectivity of over 50% for formate in the broadest range of potential regions (−0.55 to −1.05 V). In comparison, the highest selectivity of 82% is achieved for a slightly Pd-richer one ($Pd_{73}Cu_{37}$) only at −0.55V. Suitable alloy compositions and applied potentials for formate generation differ in selectivity and activity (partial current density). On the other hand, CO generation increases with increasing Cu content, and the $Pd_{44}Cu_{56}$ shows the highest selectivity and activity. In contrast to formate, the potential window for CO generation is relatively wide. The results demonstrate that the precise tuning of the alloy composition and applied potential is crucial for maximizing CO_2RR properties of bimetallic alloy NPs catalysts.

Introduction

Global warming caused by excess greenhouse gases, primarily carbon dioxide (CO_2), necessitates the reduction of their emissions and the development of effective methodologies to store and convert CO_2 into beneficial chemicals. The electrochemical CO_2 reduction reaction (CO_2RR) has been intensively studied for the conversion of CO_2 to value-added organic products, such as carbon monoxide (CO), hydrocarbons (CH_4, C_2H_4), formic acid, ethanol, and other higher carbon number compounds (n-propanol, acetate, etc.).[1-5] However, the low reaction efficiency and selectivity for the conversion of specific products hinder the commercialization of CO_2 electrolyzers; therefore, the development of catalysts[6-8] and electrolyzers[4, 9, 10] for CO_2RR, which determines both the activity and selectivity is crucial.

The improvement of activity and selectivity for CO_2RR electrocatalysts has been studied by various approaches, such as surface structure control,[11-13] halogen anion additions,[14, 15] and surface modification by organic molecules[7, 16, 17]. In addition, alloying is an effective strategy to improve the CO_2RR properties.[18-27] Not only the selectivity but also the activity and durability are improved by alloying in various alloy systems, especially in Cu-containing alloy systems such as CuAu[28, 29], CuCo[30-32], CuMo[33], and CuIn[34].

Recently, Pd-based catalysts have attracted attention as highly active and selective catalysts for converting CO_2 to formate and CO in neutral electrolytes.[35-38] Although pure Pd generates CO and formate as CO_2RR products, the competing hydrogen evolution reaction (HER) hinders the selectivity for the CO_2RR products.[39] Alloying of Pd with Cu can suppress the HER activity and simultaneously improve the selectivity for the CO_2RR products.[35, 37, 38, 40] Different studies have reported different major CO_2RR products in Pd-Cu bimetallic systems. Zhou et al. reported highly selective formate generation on two-dimensional Pd-Cu bimetallic nanodendrites, especially with a highly Pd-rich composition.[38] Similar results have been reported for dendric-structured Pd-Cu catalysts.[37] In contrast, Mun et al. achieved highly selective CO generation using Pd-Cu alloy nanoparticles with Pd:Cu ratios of 1:1 and 3:1.[35] Furthermore, mesoporous Pd-Cu catalysts with a wide range of alloy composition[40] and carbon-supported $Pd_{85}Cu_{15}$ NPs have shown similar results.[41] However, the effect of the alloy composition on the selectivity and activity is not fully understood. In addition, alloy nanostructures are often partially separated into two-

[a] Graduate School of Environmental Studies, Tohoku University, 6-2-2 Aramakiaza-Aoba Aoba-ku, Sendai 980-8579, Japan.
[b] Department of Applied Chemistry for Environment, Tokyo Metropolitan University, 1-1 Minamiosawa, Hachioji, Tokyo 192-0397, Japan.
[c] Department of Materials Science, The University of Shiga Prefecture, Hikone, Shiga 522-8533, Japan

† Footnotes relating to the title and/or authors should appear here.
Electronic Supplementary Information (ESI) available: [details of any supplementary information available should be included here]. See DOI: 10.1039/x0xx00000x

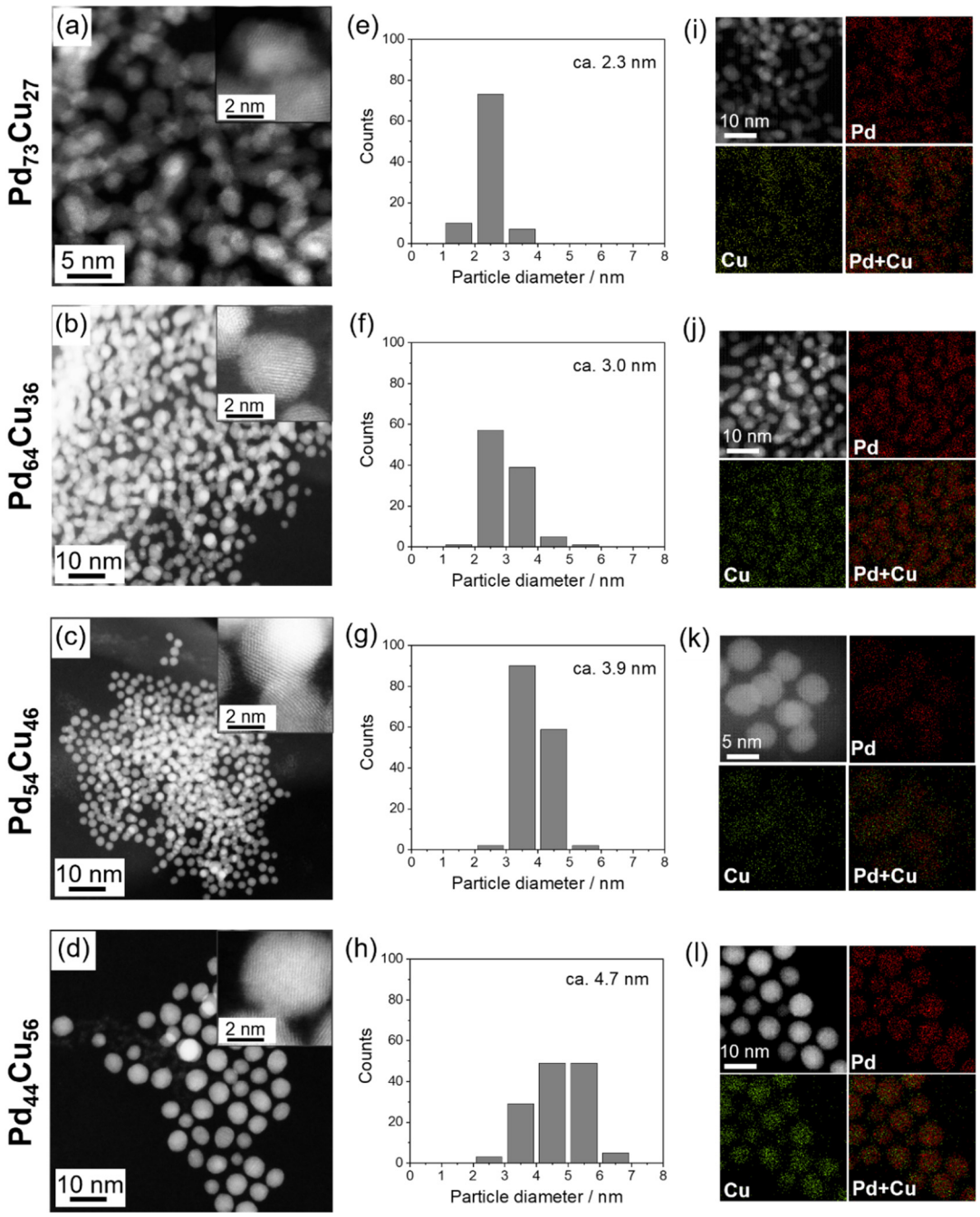

Fig. 1 (a-d) STEM images, (e-h) particle size distributions, and (i-l) STEM-EDS mappings of as-synthesized Pd-Cu alloy NPs: insets in (a-d) are high-resolution STEM images.

phase, and phase separation significantly affects the electrocatalytic performances.[42] Therefore, a more detailed investigation is needed to clarify the influence of alloy composition on the electrocatalytic properties of CO_2RR using solid-solution-alloy NPs.

In this study, we synthesized composition-controlled solid solution Pd-Cu alloy NPs by alcohol reduction method[43-46] and investigated the CO_2RR properties. All the alloy NPs exhibited enhanced selectivity for the CO_2RR compared with pure Pd and Cu particles. The Faradaic efficiency (FE) and partial current density for formate and CO were summarized against the alloy composition and the applied potentials. Then, the influence of alloy composition was discussed by comparing it with previous reports. The $Pd_{64}Cu_{36}$ presents a selectivity of over 50% for formate in the broadest range of potential regions. In comparison, the highest selectivity of 82% is achieved for a

slightly Pd-richer one ($Pd_{73}Cu_{37}$) only at −0.55V. The results indicate that control of both the alloy composition and applied potential is vital for maximizing the electrocatalyst performance for CO_2RR.

Experimental

Synthesis of Pd-Cu alloy nanoparticles

To synthesize Pd-Cu alloy nanoparticles, 100 mL of 1-heptanol as a reducing solvent was placed in a separable four-neck flask, and then palladium (II) acetate (Aldrich, 98 %) and anhydrous copper (II) acetate (Fujifilm, 97 %) as metallic precursors were added so that the total concentration was 0.05 mmol. Subsequently, 20 mmol of oleylamine (Aldrich, 98 %) was added as a surfactant. The solution was then heated from room temperature to 120 °C for 20 min and then maintained at this temperature for 30 min, subsequently raising the temperature to 172 °C at a heating rate of 4.5 °C min^{-1}. The solution was refluxed at 172 °C for 3 h. After the reaction, the solution was allowed to cool to room temperature. The nanoparticles were collected by centrifugation and redispersed in acetone by ultrasonication. This process was repeated three times, and the collected particles were suspended in toluene. Additionally, pure Pd and Cu nanoparticles were synthesized using the same procedure.

Preparation of working electrodes

To prepare the catalyst ink, 5 mg of the catalyst powder was added to a mixture of 960 µL of isopropanol (Fujifilm, 98 %) and 40 µL of Nafion solution (Fujifilm, 5 wt.%). The mixture was then ultrasonicated for 30 min to form homogeneous ink. The catalyst ink was drop-casted to the gas diffusion layer (SGL, SIGRACET39BB) at 60 °C and dried in a vacuum desiccator overnight. The catalyst loading was fixed at 1.2 mg cm^{-2}.

Electrochemical measurement and CO_2RR product analysis

A potentiostat−galvanostat (SP-50eZ, Biologic) equipped with an impedance module was used for the electrochemical measurements. An H-type glass cell, a Pt wire, and a reversible hydrogen electrode (RHE) were employed as the electrochemical (EC) cell, counter electrode, and reference electrode, respectively. The anode and cathode compartments (15 mL each) were separated using a Nafion membrane (NR212; Chemours). All electrochemical measurements were performed in 0.5 M $KHCO_3$ solution at 20 °C. The solution was prepared using $KHCO_3$ powder (>99%, ACS grade, Merck) and ultrapure water (Milli-Q). The electrode areas exposed to the electrolyte were fixed to 1 cm^2. The measured currents were normalized by the geometrical surface area.

After the cyclic voltammetry between 0 and -1.0 V for surface cleaning, CO_2 gas (>99.995%) was purged into the electrolyte at a constant flow rate of 50 mL min^{-1} using a mass flow controller (S48-32, HORIBA STEC) during the CO_2RR electrolysis measurements. Constant-potential electrolysis was performed for 10 min, and the generated gaseous products of CO_2 reduction were analyzed by gas chromatography (GC; GC-2014, Shimadzu) using a thermal conductivity detector, flame ionization detector, and methanizer (MTN-1, Shimadzu). The liquid products were analyzed by nuclear magnetic resonance (NMR) spectroscopy (JEOL, ECZL-600). The 0.5 mL of the electrolyte containing CO_2 reduction products after the electrolysis was mixed with 0.5 µL of dimethyl sulfoxide (DMSO) and 0.1 mL of D_2O for NMR analysis. Standard curves of liquid products were made using purchased chemicals (Fujifilm) with the internal standards DMSO in 0.5 M $KHCO_3$. The water peak was suppressed by a pre-saturation sequence. The faradaic efficiency was calculated using the following equation:

$$FE\ (\%) = (nF \times z)Q \times 100$$

where *n* is the amount of a specific product estimated from GC and NMR, *z* is the number of electrons required to generate one molecule of a specific product, *F* is the Faradaic constant (96,500 C mol^{-1}), and Q is the total amount of charge passed during constant potential electrolysis.

Characterization

The crystal structures of the alloy nanoparticles were analyzed using X-ray diffraction (XRD; RINT2000, Rigaku). The d-spacing (*d*) was calculated using Bragg's law ($\lambda = 2dsin\theta$; $\lambda\ (CuK\alpha) = 0.15418\ nm$). Scanning transmission electron microscopy (STEM; ARM200F NEOARM, JEOL) with energy-dispersive X-ray spectroscopy (EDS) was used to observe the microstructures and estimate alloy compositions. The surface chemical bonding states were analyzed using X-ray photoelectron spectroscopy (XPS; JPS-9010MX, SHIMADZU) with a Mg Kα X-ray source.

Results

The STEM images of the as-prepared Pd-Cu alloy NPs are summarized in Fig.1. The STEM images (Fig.1(a-d)) show that spherical NPs are synthesized regardless of the alloy composition. However, the necking structures are more prominent for $Pd_{73}Cu_{27}$ than for the other alloy NPs. The particle size distributions estimated from the STEM images (Fig.1(e-h)) show that the mean diameter gradually increases with increasing Cu content. The corresponding STEM-EDS mappings of Pd and Cu show that the two metal elements are uniformly present in each particle, with no segregated phases of pure Pd and Cu.

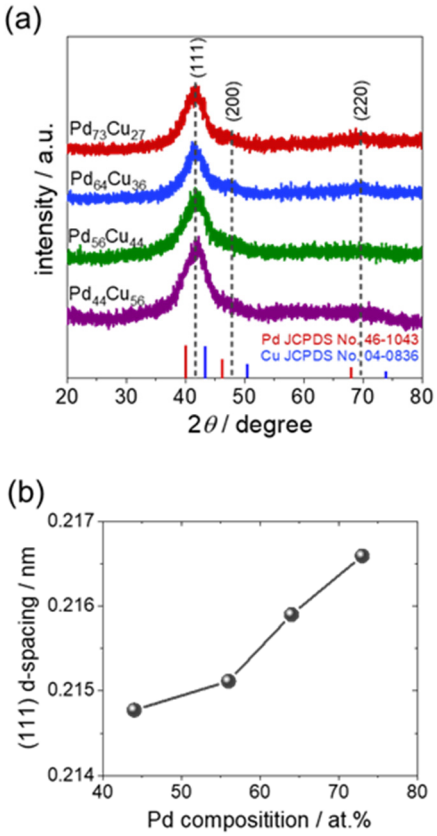

Fig. 2 (a) XRD patterns of as-synthesized Pd-Cu alloy nanoparticles; (b) d-spacings of (111) plane of Pd-Cu NPs as a function of the Pd content.

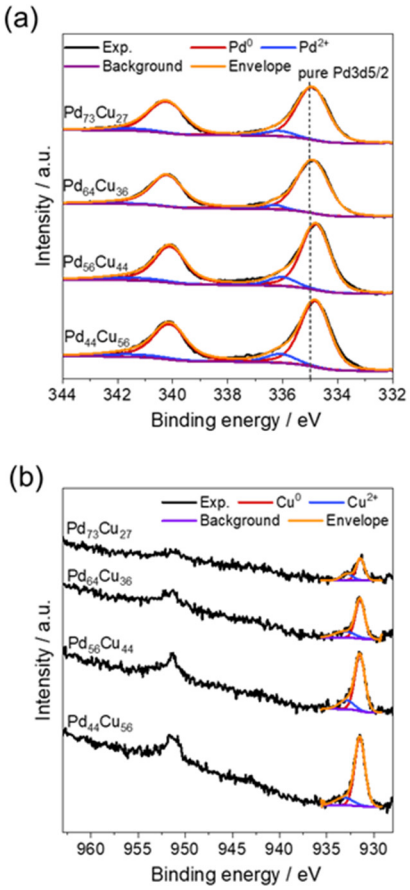

Fig. 3 XPS spectra of Pd3d (a) and Cu2p (b) orbitals of as-synthesized Pd-Cu alloy nanoparticles.

The XRD patterns of the as-synthesized Pd-Cu NPs are shown in Fig. 2(a). All alloy NPs exhibit a distinct (111) peak at approximately 42°, with broad (200) and (220) peaks at 47.6° and 69.6°, respectively. The positions of the (111), (200), and (220) peaks of the alloy NPs are located between the corresponding peaks of pure Cu (JCPDS 04–0836) and Pd (46–1043). Furthermore, the alloy NPs show no phase separation peaks of pure Pd and Cu, indicating that the elements are well-mixed within solid-solution (alloy) NPs, which is consistent with the STEM-EDS results. The d-spacing of the (111) plane increases with increasing Pd content from Cu-rich ($Cu_{46}Pd_{54}$) to Pd-rich NPs ($Cu_{73}Pd_{27}$), suggesting that the crystal lattice constant varies with the alloy composition (Fig.2(b)).

Fig.3 shows the XPS spectra of Pd3d and Cu2p bands of the as-synthesized Pd-Cu alloy nanoparticles. Both spectra indicate that the metallic components (Pd^0 and Cu^0) are dominant, implying that all the as-synthesized NPs have metallic surface states regardless of the alloy composition. As for the Pd3d orbital, the peak position of the Pd3d5/2 band at 335.0 eV for $Pd_{73}Cu_{27}$ NPs is in good agreement with that of the pure Pd NPs[47]. The peaks of the Pd-Cu alloy NPs gradually shift to lower binding energies with an increase in the Cu content, and the chemical shift is approximately 0.2 eV for $Pd_{44}Cu_{56}$ NPs. This chemical shift can be attributed to charge transfer between Pd and Cu[48, 49], and this effect is likely to be enhanced by increasing the Cu content in the alloy NPs.

Figs. 4a-4c show the FEs of the Pd-Cu, pure Pd, and Cu NPs for formate, CO, and H_2. Hydrocarbons (CH_4 and C_2H_4) are detected as the CO_2RR products of Pd-Cu NPs at low potential ranges (<−0.95 V); however, their dependence on alloy composition is not discussed because they are minor products (see Fig. S1 in the Supplementary Information). As shown in Fig. 4a-4c, the FE of all Pd-Cu NPs for formate increased more compared with that of pure Pd and Cu NPs. The improvement of the FE in low potential regions (−0.57 to −0.78 V) is significant, which agrees well with those in previous studies on Pd-Cu bimetallic nanostructures.[37, 38] In particular, the $Pd_{64}Cu_{36}$ shows more than 50% FE in a wide potential range from −0.57 to −1.05 V, whereas the highest FE is lower than that of the $Pd_{73}Cu_{27}$. In contrast, the FE for CO is highly dependent on the alloy composition and the applied potential. However, the FE of only

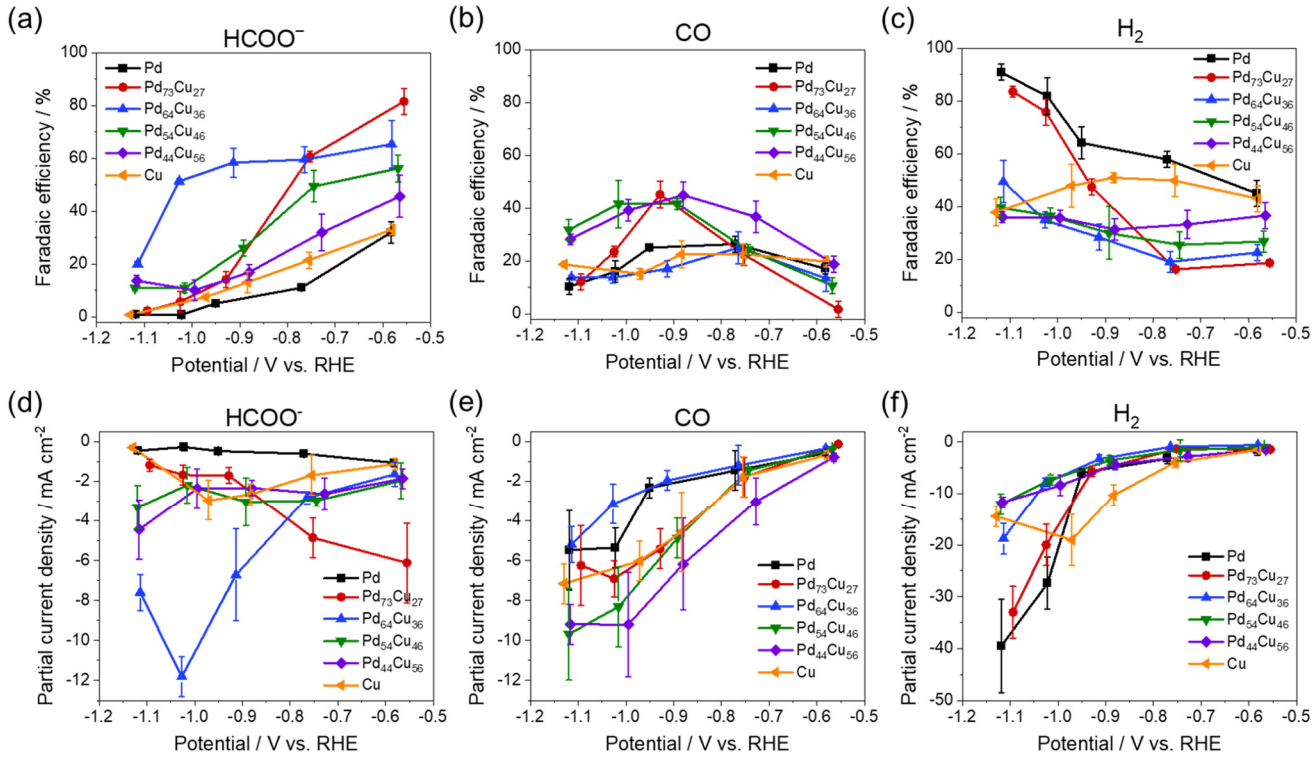

Fig. 4 Faradaic efficiencies (a-c) and partial current densities (d-e) of Pd-Cu alloy, Pd and Cu nanoparticles for formate, CO, and H_2 measured in CO_2-saturated 0.5 M $KHCO_3$.

$Pd_{44}Cu_{56}$ increases in the whole potential range except at −0.56 V. For H_2, the overall FE of the Pd-Cu NPs decreases compared with that of pure Pd. Therefore, in the case of solid-solution alloy NPs, alloying Pd with Cu is effective in improving the selectivity for CO_2RR products, especially for formate.

The partial current densities of the CO_2RR products are shown in Fig.4d-4e. The linear sweep voltammetry curves (Fig. S3a) show that the current density increases with increasing Cu content for the Pd-Cu alloy NPs in the potential region. The partial current density for formate is considerably larger for $Pd_{64}Cu_{36}$ than that for other samples in the potential regions below −0.9 V. Whereas, $Pd_{73}Cu_{27}$ is the largest in the potential regions above −0.8 V. In contrast, all the Pd-Cu NPs except $Pd_{64}Cu_{36}$ exhibit an increase in the partial current density for CO. For H_2, $Pd_{73}Cu_{27}$ and pure Pd show similar HER activity; however, a greater increase in the Cu content in the Pd-Cu NPs reduces the activity compared to those in pure Pd and Cu. These results suggest that fine-tuning the alloy composition and applied potential is crucial for obtaining the best catalytic performance of Pd-Cu NPs.

To understand the relationship between the CO_2RR properties, alloy composition, and applied potentials, we constructed contour maps of the FE and partial current density for formate and CO (Fig.5). Fig.5a shows that the high FE of more than 70% for formate can be achieved only in a considerably narrow range of potential (approximately −0.6V) and composition (73 at. % Pd). In contrast, the relatively high FE can be maintained at low potentials down to −1.05 V by decreasing the Pd composition to 64 at. %, although the FE drops to 50-60%. With respect to the partial current density (Fig. 5b), the highest partial current density (performance) for formate is obtained in a narrower potential and composition range than that for FE. In contrast, for CO, relatively high FE regions (>40%, light green) are distributed over wide potential and alloy composition ranges (Fig. 3c). Similarly, the partial current density is also widely distributed. However, the region of maximum values shown in orange is narrower than that of FE for CO. Accordingly, the results indicate that the best selectivity and activity for formate are achieved at different compositions and potential ranges. In contrast, the composition dependence of selectivity and activity for formate is relatively small compared to CO.

Discussion

These results suggest that the potential and composition-dependent CO_2RR properties of Pd-Cu alloy NPs vary significantly, depending on the reduction products. Table S1 shows the FEs and partial current densities of formate and CO for the previously reported nanostructured Pd-Cu bimetallic alloy catalysts. The reported alloy catalysts exhibit high

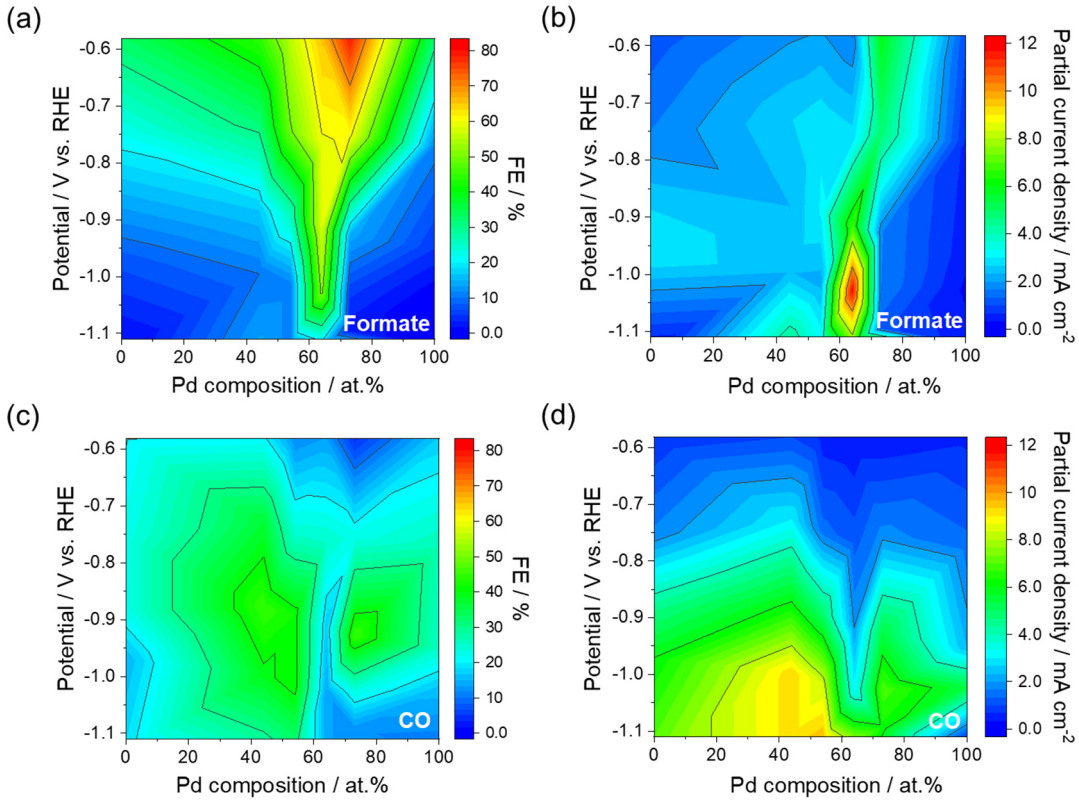

Fig. 5 Contour plots of faradaic efficiency and partial current density versus Pd composition and applied potential: (a, b) formate and (c, d) CO.

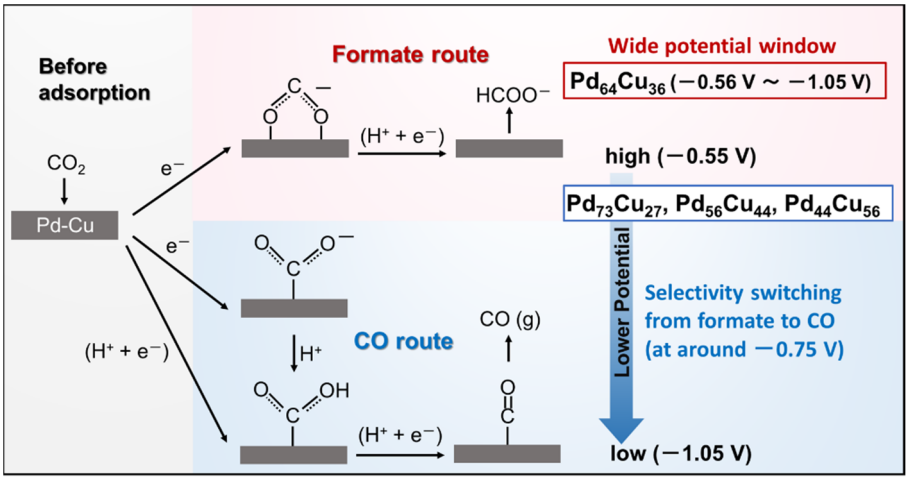

Fig. 6 Schematic of the reaction steps for formate and CO generation through CO_2RR, and the influence of alloy composition and applied potential.

selectivity only for formate (nanodendrites[38] and dendritic porous structures[37]) or CO (carbon-supported nanoparticles[35, 41] and mesoporous nanostructures[40]). In contrast, the Pd-Cu alloy NPs synthesized in this study exhibited some degree of selectivity for CO, whereas the highest FE was obtained for formate, regardless of the alloy composition. In particular, $Pd_{54}Cu_{46}$ and $Pd_{44}Cu_{66}$, whose Cu compositions were above 50%, showed selectivity of more than 40% for CO, and the values exceeded those for formate.

Although previous studies on Pd-Cu-alloy catalysts have investigated the influence of alloy composition on product selectivity, composition-dependent selectivity trends and

changes in the potential window have not been reported. The reaction pathway of the CO_2RR for formate or other products with CO as an intermediate species is determined by the adsorption alignment of CO_2 in the first reaction step of the CO_2RR[50] as shown in Fig.6. In the first reaction step, the CO_2 molecule is adsorbed as CO_2^- onto the electrocatalyst surface via electron transfer from the surface. Here, the two oxygen atoms are oriented toward the electrocatalyst surface in the formate formation pathway, whereas the carbon atom is oriented toward the surface in the CO pathway. Accordingly, in this study, the adsorption orientation of CO_2 was altered by varying the alloy composition and applied potentials of the Pd-Cu NPs. Gao et al. have demonstrated that the selectivity of Pd NPs changes from formate to CO by lowering the applied potential.[51] Additionally, they have deduced that the potential dependent selectivity change is derived from different surface states using in-situ X-ray absorption spectroscopy technique and density functional theory calculations; hydrogen-absorbed α+β PdH_x surface in the high potential region (higher than -0.3 V vs RHE) stabilizes the O-down CO_2 as a formate intermediate, whereas metallic Pd surface leads the C-down CO_2 adsorption, resulting in CO formation. Although the influence of such surface hydrogenation on selectivity has not been demonstrated for Pd-Cu-alloy catalysts, it might affect the selectivity because hydrogen absorption reactions can occur on Pd-Cu alloys.[52] Specifically, the preferential CO_2RR products of $Pd_{73}Cu_{27}$, $Pd_{56}Cu_{44}$, and $Pd_{44}Cu_{56}$ change from formate to CO at approximately −0.75 V. In contrast, only $Pd_{64}Cu_{36}$ showed higher formate selectivity than CO at all applied potentials. This study cannot explain the large difference in potential-dependent selectivity at only a 10% difference in composition. Elucidating this composition effect is challenging for nanostructured catalysts because the selectivity is also influenced by several factors including the surface atomic structures[12, 13, 53] and lattice strain[54, 55]. Studies using model catalysts such as single-crystal electrodes with well-defined surface structures can be a potential tool for clarifying this issue.

Conclusions

In this study, the CO_2RR properties of Pd-Cu bimetallic NPs synthesized by alcohol reduction were investigated using neutral electrolytes. All Pd-Cu NPs exhibited spherical solid-solution alloy structures without the formation of segregated phases of pure Pd and Cu. Formate and CO were the main CO_2RR products, regardless of alloy composition. However, the selectivity and activity depended significantly on the alloy composition and applied potential. The $Pd_{64}Cu_{36}$ alloy exhibited a selectivity of more than 50% for formate over a wide range of applied potentials, whereas it was highest (82%) for the Pd-richer alloy ($Pd_{73}Cu_{37}$). Considering the effect of composition in this study, the suitable chemical composition of the Pd-Cu NPs and the applied potential for formate generation were different in terms of selectivity and activity. However, CO generation improved with increasing Cu content, and $Pd_{44}Cu_{56}$ exhibited the highest selectivity and activity. In contrast to formate, the potential window for CO generation was relatively wide. These results indicate that the alloy composition and applied potential should be fine-tuned to maximize the CO_2RR properties of Pd-Cu-alloy NP catalysts.

Conflicts of interest

There are no conflicts to declare.

Acknowledgments

This study was partially supported by JST, PRESTO Grand Number JPMJPR20T3 (N.T.), Japan. M.I. would like to thank Mr. Ono of Tokyo Metropolitan University for providing valuable technical support during HAADF-STEM observations.

Notes and references

1. S. C. Perry, P.-k. Leung, L. Wang and C. Ponce de León, *Curr. Opin. Electrochem.*, 2020, **20**, 88-98.
2. J. Xie, Y. Huang, M. Wu and Y. Wang, *ChemElectroChem*, 2019, **6**, 1-19.
3. I. E. L. Stephens, K. Chan, A. Bagger, S. W. Boettcher, J. Bonin, E. Boutin, A. K. Buckley, R. Buonsanti, E. R. Cave, X. Chang, S. W. Chee, A. H. M. da Silva, P. de Luna, O. Einsle, B. Endrődi, M. Escudero-Escribano, J. V. Ferreira de Araujo, M. C. Figueiredo, C. Hahn, K. U. Hansen, S. Haussener, S. Hunegnaw, Z. Huo, Y. J. Hwang, C. Janáky, B. S. Jayathilake, F. Jiao, Z. P. Jovanov, P. Karimi, M. T. M. Koper, K. P. Kuhl, W. H. Lee, Z. Liang, X. Liu, S. Ma, M. Ma, H.-S. Oh, M. Robert, B. R. Cuenya, J. Rossmeisl, C. Roy, M. P. Ryan, E. H. Sargent, P. Sebastián-Pascual, B. Seger, L. Steier, P. Strasser, A. S. Varela, R. E. Vos, X. Wang, B. Xu, H. Yadegari and Y. Zhou, *JPhys Energy*, 2022, **4**, 042003.
4. M. Sassenburg, R. de Rooij, N. T. Nesbitt, R. Kas, S. Chandrashekar, N. J. Firet, K. Yang, K. Liu, M. A. Blommaert, M. Kolen, D. Ripepi, W. A. Smith and T. Burdyny, *ACS Appl Energy Mater*, 2022, **5**, 5983-5994.
5. X. Tan, C. Yu, Y. Ren, S. Cui, W. Li and J. Qiu, *Energ. Environ. Sci.*, 2021, **14**, 765-780.
6. B. Zhang, Y. Jiang, M. Gao, T. Ma, W. Sun and H. Pan, *Nano Energy*, 2021, **80**, 105504.
7. D.-H. Nam, P. De Luna, A. Rosas-Hernández, A. Thevenon, F. Li, T. Agapie, J. C. Peters, O. Shekhah, M. Eddaoudi and E. H. Sargent, *Nat. Mat.*, 2020, **19**, 266-276.
8. K. A. Adegoke, R. O. Adegoke, A. O. Ibrahim, S. A. Adegoke and O. S. Bello, *Sustainable Materials and Technologies*, 2020, **25**, e00200.
9. Z. Xing, L. Hu, D. S. Ripatti, X. Hu and X. Feng, *Nat. Commun.*, 2021, **12**, 136.
10. D. Higgins, C. Hahn, C. Xiang, T. F. Jaramillo and A. Z. Weber, *ACS Energy Lett.*, 2019, **4**, 317-324.
11. Y. Hori, I. Takahashi, O. Koga and N. Hoshi, *Journal of Molecular Catalysis A: Chemical*, 2003, **199**, 39-47.

12. N. Todoroki, H. Tei, H. Tsurumaki, T. Miyakawa, T. Inoue and T. Wadayama, *ACS Catal.*, 2019, **9**, 1383-1388.
13. N. Todoroki, H. Tei, T. Miyakawa, H. Tsurumaki and T. Wadayama, *ChemElectroChem*, 2019, **6**, 3101-3107.
14. W. Ma, S. Xie, T. Liu, Q. Fan, J. Ye, F. Sun, Z. Jiang, Q. Zhang, J. Cheng and Y. Wang, *Nat. Catal.*, 2020, **3**, 478-487.
15. H. Lu, L. Li, Q. Wu, S. Mu, R. Zhao, X. Zheng, C. Long, Q. Li, H. Liu and C. Cui, *ACS Appl. Mater.*, 2023, **15**, 13228-13237.
16. C. Yang, S. Li, Z. Zhang, H. Wang, H. Liu, F. Jiao, Z. Guo, X. Zhang and W. Hu, *Small*, 2020, **16**, 2001847.
17. S. Yoshida, M. Sampei, N. Todoroki, E. Hisamura, K. Nakao, K. Albrecht and T. Wadayama, *Chem. Commun.*, 2023, **59**, 3459-3462.
18. Z. Zhao and G. Lu, *ACS Catal.*, 2018, **8**, 3885-3894.
19. J. He, N. J. J. Johnson, A. Huang and C. P. Berlinguette, 2018, **11**, 48-57.
20. K. Iwase, T. Kojima, N. Todoroki and I. Honma, *Chem. Commun.*, 2022, **58**, 4865-4868.
21. C. W. Lee, K. D. Yang, D.-H. Nam, J. H. Jang, N. H. Cho, S. W. Im and K. T. Nam, *Adv. Mater.*, 2018, **30**, 1704717.
22. T. K. Todorova, M. W. Schreiber and M. Fontecave, *ACS Catal.*, 2020, **10**, 1754-1768.
23. X. Su, Y. Sun, L. Jin, L. Zhang, Y. Yang, P. Kerns, B. Liu, S. Li and J. He, *Appl. Catal., B*, 2020, **269**, 118800.
24. Y. Feng, W. An, Z. Wang, Y. Wang, Y. Men and Y. Du, *ACS Sustain. Chem. Eng.*, 2020, **8**, 210-222.
25. J. Hao, H. Zhu, Q. Zhao, J. Hao, S. Lu, X. Wang, F. Duan and M. Du, *Nano Research*, 2023, DOI: 10.1007/s12274-023-5577-2.
26. J. Hao, Z. Zhuang, J. Hao, K. Cao, Y. Hu, W. Wu, S. Lu, C. Wang, N. Zhang, D. Wang, M. Du and H. Zhu, *ACS Nano*, 2022, **16**, 3251-3263.
27. J. Hao, H. Zhu, Y. Li, P. Liu, S. Lu, F. Duan, W. Dong, Y. Lu, T. Liu and M. Du, *Chem. Eng.*, 2021, **404**, 126523.
28. J. W. Vickers, D. Alfonso and D. R. Kauffman, *Energy Technol.*, 2017, **5**, 775-795.
29. D. Kim, J. Resasco, Y. Yu, A. M. Asiri and P. Yang, *Nat. Commun.*, 2014, **5**, 4948.
30. C. Dai, L. Sun, J. Song, H. Liao, A. C. Fisher and Z. J. Xu, *Small Methods*, 2019, **3**, 1900362.
31. M. Bernal, A. Bagger, F. Scholten, I. Sinev, A. Bergmann, M. Ahmadi, J. Rossmeisl and B. R. Cuenya, *Nano Energy*, 2018, **53**, 27-36.
32. J. Ahmed, A. Ganguly, S. Saha, G. Gupta, P. Trinh, A. M. Mugweru, S. E. Lofland, K. V. Ramanujachary and A. K. Ganguli, *J. Phys. Chem. C*, 2011, **115**, 14526-14533.
33. Z. Zhang, J. Hu, X. Zheng, W. Zhang, S. Lu, F. Duan, H. Zhu and M. Du, *Chem Commun (Camb)*, 2023, **59**, 5221-5224.
34. S. Rasul, D. H. Anjum, A. Jedidi, Y. Minenkov, L. Cavallo and K. Takanabe, *Angewandte Chemie*, 2015, **127**, 2174-2178.
35. Y. Mun, S. Lee, A. Cho, S. Kim, J. W. Han and J. Lee, *Appl. Catal., B*, 2019, **246**, 82-88.
36. T. Takashima, T. Suzuki and H. Irie, *Electrochemistry*, 2019, **87**, 134-138.
37. Y. Sun, F. Wang, F. Liu, S. Zhang, S. Zhao, J. Chen, Y. Huang, X. Liu, Y. Wu and Y. Chen, *ACS Appl. Mater.*, 2022, **14**, 8896-8905.
38. R. Zhou, X. Fan, X. Ke, J. Xu, X. Zhao, L. Jia, B. Pan, N. Han, L. Li, X. Liu, J. Luo, H. Lin and Y. Li, *Nano Lett.*, 2021, **21**, 4092-4098.
39. D. Gao, H. Zhou, F. Cai, J. Wang, G. Wang and X. Bao, *ACS Catal.*, 2018, **8**, 1510-1519.
40. M. Li, J. Wang, P. Li, K. Chang, C. Li, T. Wang, B. Jiang, H. Zhang, H. Liu, Y. Yamauchi, N. Umezawa and J. Ye, *J. Mater. Chem. A*, 2016, **4**, 4776-4782.
41. Z. Yin, D. Gao, S. Yao, B. Zhao, F. Cai, L. Lin, P. Tang, P. Zhai, G. Wang, D. Ma and X. Bao, *Nano Energy*, 2016, **27**, 35-43.
42. S. Ma, M. Sadakiyo, M. Heima, R. Luo, R. T. Haasch, J. I. Gold, M. Yamauchi and P. J. Kenis, *J. Am. Chem. Soc.*, 2017, **139**, 47-50.
43. M. Ishijima, J. L. Cuya Huaman, H. Wakizaka, K. Suzuki, H. Miyamura and J. Balachandran, *Inorg. Chem.*, 2021, **60**, 14436-14445.
44. M. Ishijima, T. Matsumoto, J. L. Cuya Huaman, K. Shinoda, M. Uchikoshi, K. Matsuo, K. Suzuki, H. Miyamura and J. Balachandran, *Inorg. Chem.*, 2021, **60**, 9432-9441.
45. M. Ishijima, J. L. Cuya Huaman, S. Yokoyama, K. Shinoda, M. Uchikoshi, H. Miyamura and B. Jeyadevan, *New Journal of Chemistry*, 2018, **42**, 13044-13053.
46. M. Ishijima, T. Takada, J. L. Cuya Huaman, T. Mizutomi, O. Sakai, K. Shinoda, M. Uchikoshi, H. Mamiya, K. Suzuki, H. Miyamura and J. Balachandran, *Inorg. Chem.*, 2022, **61**, 17144-17153.
47. M. Iqbal, C. Li, B. Jiang, M. S. A. Hossain, M. T. Islam, J. Henzie and Y. Yamauchi, *J. Mater. Chem. A*, 2017, **5**, 21249-21256.
48. K. E. Salnikova, Y. V. Larichev, E. M. Sulman, A. V. Bykov, A. I. Sidorov, G. N. Demidenko, M. G. Sulman, L. M. Bronstein and V. G. Matveeva, *ChemPlusChem*, 2020, **85**, 1697-1703.
49. Q. Liu, Z. Li, X. Zhou, J. Xiao, Z. Han, X. Jiang, G. Fu and Y. Tang, *Advanced Energy and Sustainability Research*, 2022, **3**, 2200067.
50. Y. Wu, S. Cao, J. Hou, Z. Li, B. Zhang, P. Zhai, Y. Zhang and L. Sun, *Adv. Energy Mater.*, 2020, **10**, 2000588.
51. D. Gao, H. Zhou, F. Cai, D. Wang, Y. Hu, B. Jiang, W.-B. Cai, X. Chen, R. Si, F. Yang, S. Miao, J. Wang, G. Wang and X. Bao, *Nano Research*, 2017, **10**, 2181-2191.
52. K. Xuezhi, K. Gert Jan and L. Ole Martin, *Journal of Physics: Condensed Matter*, 2004, **16**, 6267.
53. N. Todoroki, N. Yokota, S. Nakahata, H. Nakamura and T. Wadayama, *Electrocatalysis*, 2016, **7**, 97-103.
54. M. Du, X. Zhao, G. Zhu, H.-Y. Hsu and F. Liu, *J. Mater. Chem. A*, 2021, **9**, 4933-4944.
55. R. P. Jansonius, L. M. Reid, C. N. Virca and C. P. Berlinguette, *ACS Energy Lett.*, 2019, **4**, 980-986.

